

# Emergence of Interlayer Coherence in Twist-Controlled Graphene Double Layers

Kenneth A. Lin,<sup>1</sup> Nitin Prasad,<sup>2</sup> G. William Burg,<sup>1</sup> Bo Zou,<sup>3</sup> Keiji Ueno,<sup>4</sup> Kenji Watanabe,<sup>5</sup> Takashi Taniguchi,<sup>6</sup> Allan H. MacDonald,<sup>3</sup> and Emanuel Tutuc<sup>1,\*</sup>

<sup>1</sup>*Microelectronics Research Center, Department of Electrical and Computer Engineering, The University of Texas at Austin, Austin, TX 78758, USA*

<sup>2</sup>*Department of Chemistry and Biochemistry, University of Maryland, College Park, MD 20742, USA*

<sup>3</sup>*Department of Physics, The University of Texas at Austin, Austin, Texas 78712, USA*

<sup>4</sup>*Department of Chemistry, Graduate School of Science and Engineering, Saitama University, Saitama 338-8570, Japan*

<sup>5</sup>*Research Center for Functional Materials, National Institute of Materials Science, 1-1 Namiki Tsukuba, Ibaraki 305-0044, Japan*

<sup>6</sup>*International Center for Materials Nanoarchitectonics, National Institute of Materials Science, 1-1 Namiki Tsukuba, Ibaraki 305-0044, Japan*

(Dated: November 22, 2022)

We report enhanced interlayer tunneling with reduced linewidth at zero interlayer bias in a twist-controlled double monolayer graphene heterostructure in the quantum Hall regime, when the top ( $\nu_T$ ) and bottom ( $\nu_B$ ) layer filling factors are near  $\nu_T = \pm 1/2, \pm 3/2$  and  $\nu_B = \pm 1/2, \pm 3/2$ , and the total filling factor  $\nu = \pm 1$  or  $\pm 3$ . The zero-bias interlayer conductance peaks are stable against variations of layer filling factor, and signal the emergence of interlayer phase coherence. Our results highlight twist control as a key attribute in revealing interlayer coherence using tunneling.

In closely spaced double layer systems placed in the quantum Hall regime, the interlayer and intralayer interactions lead to ground states not present in single layers, including even denominator fractional quantum Hall states (QHSs) at total Landau level (LL) filling  $\nu = 1/2$  and  $1/4$  [1–4], as well as  $\nu = 1$  states that are interlayer electron-hole pair condensates [5] with enhanced interlayer coherence. Experimental evidence for this phenomenon in GaAs double layers includes Josephson-like interlayer tunneling [6–8], counterflow with near zero dissipation [9–12], and Andreev reflection [13]. In graphene double layers, quantized Hall drag [14] and counterflow [15] measurements have provided evidence of particle-hole pairing at total filling factor  $\nu = 1$  and  $\nu = 3$ . Here, we investigate interlayer tunneling in a twist-controlled double monolayer graphene heterostructure, where tunneling in the quantum Hall effect regime provides insight into interlayer phase coherence. We observe enhanced interlayer tunneling at zero interlayer bias at  $\nu = \pm 1$  and  $\pm 3$  that is immune to changes in individual layer filling factors, a fingerprint of nascent interlayer phase coherence.

Figure 1(a) shows a schematic of the twist-controlled double monolayer graphene-hBN heterostructure, which consists of two rotationally aligned and independently contacted graphene monolayers separated by a  $d = 2$  nm thick hBN tunnel barrier. Top and bottom hBN dielectrics encapsulate the heterostructure [16], and top ( $V_{TG}$ ) and bottom ( $V_{BG}$ ) graphite gate biases tune the layers densities. The crystal axis alignment of the two graphene layers [17] establishes energy and momentum conserving interlayer tunneling [18–21], which leads to interlayer voltage-current characteristics with gate tunable negative differential resistance (NDR), and provides sensitivity to interlayer phase coherence. Multiple con-

tacts to each graphene layer allow four-point interlayer current ( $I_{Int}$ ) vs. interlayer voltage ( $V_{Int}$ ) measurements to decouple interlayer tunneling characteristics from contact resistances. Figure 1(b) shows an optical micrograph of the heterostructure.

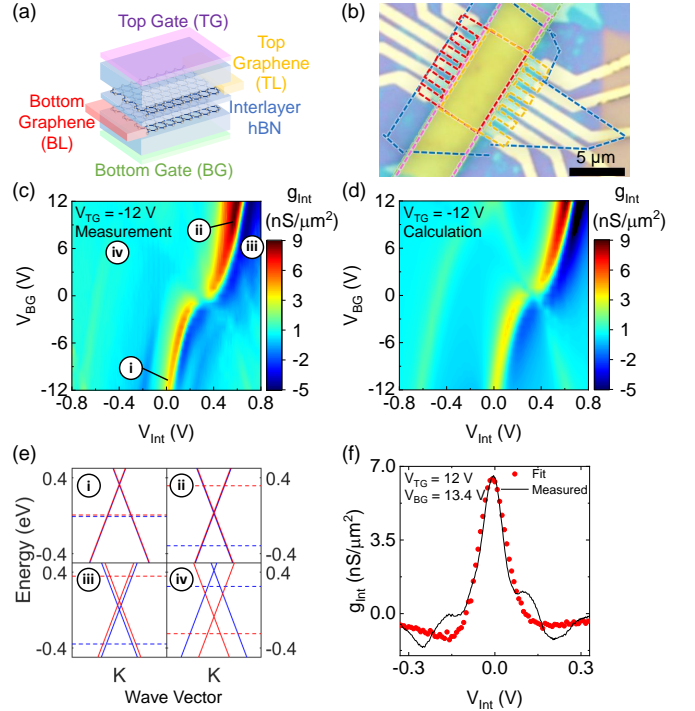


FIG. 1. (a) Schematic and (b) optical micrograph of a graphene double layer. (c) Experimental and (d) calculated  $g_{Int}$  vs.  $V_{Int}$  and  $V_{BG}$  at  $T = 1.5$  K for  $V_{TG} = -12$  V. (e) Band alignment of top (red) and bottom (blue) graphene for the biasing points labeled in (c). The dashed lines indicate the layer Fermi levels. (f) Experimental (line) and calculated (dots)  $g_{Int}$  vs.  $V_{Int}$  at  $V_{TG} = 12$  and  $V_{BG} = 13.4$  V.

Figure 1(c) shows the interlayer conductance  $g_{\text{Int}} = dI_{\text{Int}}/dV_{\text{Int}}$  vs.  $V_{\text{Int}}$  and  $V_{\text{BG}}$ , measured at a top gate bias of  $V_{\text{TG}} = -12$  V, temperature  $T = 1.5$  K;  $V_{\text{Int}}$  is applied on the top layer, while the bottom layer is held at ground. The data show resonant tunneling manifested by a  $g_{\text{Int}}$  peak and NDR, which evolve with  $V_{\text{Int}}$  and  $V_{\text{BG}}$ , and correspond to the biasing condition where the layers energy bands are aligned, indicating energy and momentum conserving tunneling. We can explain the interlayer tunneling characteristics using a single-particle model [21, 22],

$$I_{\text{Int}} = -e \int_{-\infty}^{\infty} T(E) [f_{\text{T}}(E) - f_{\text{B}}(E)] dE \quad (1)$$

where  $E$  is the energy,  $f_{\text{T}}$  ( $f_{\text{B}}$ ) is the state occupancy in the top (bottom) layer, and  $e$  the elementary charge. The tunneling rate [ $T(E)$ ] is given by

$$T(E) = \frac{2\pi}{\hbar} \sum_{\mathbf{k};s,s'} |t|^2 A_{\text{T}}(\mathbf{k}, E) A_{\text{B}}(\mathbf{k}, E) \quad (2)$$

where  $t$  is the interlayer coupling, and  $A_{\text{T,B}}(\mathbf{k}, E)$  the spectral density in the top and bottom layers is assumed to be Lorentzian,

$$A_{\text{T,B}}(\mathbf{k}, E) = \frac{1}{\pi} \frac{\Gamma}{(E - \epsilon_{\text{T,B}}(\mathbf{k}))^2 + \Gamma^2} \quad (3)$$

where  $\epsilon_{\text{T,B}}(\mathbf{k})$  is the top, bottom graphene energy-momentum dispersion, respectively, and  $\Gamma$  the quasiparticle state energy broadening, assumed to be the same in both layers. The top (bottom) graphene layer density  $n_{\text{T}}$  ( $n_{\text{B}}$ ) is calculated using the following set of equations:

$$V_{\text{BG}} C_{\text{BG}} + C_{\text{TG}}(V_{\text{TG}} - V_{\text{Int}}) = e(n_{\text{T}} + n_{\text{B}}) + \frac{\mu_{\text{B}} C_{\text{BG}} + \mu_{\text{T}} C_{\text{TG}}}{e} \quad (4)$$

$$V_{\text{TG}} C_{\text{TG}} - V_{\text{Int}}(C_{\text{TG}} + C_{\text{Int}}) = en_{\text{T}} + \frac{\mu_{\text{T}}}{e}(C_{\text{Int}} + C_{\text{TG}}) - \frac{\mu_{\text{B}}}{e} C_{\text{Int}} \quad (5)$$

where  $C_{\text{TG}}$  ( $C_{\text{BG}}$ ) is the top (bottom) gate capacitance,  $C_{\text{Int}}$  the interlayer capacitance,  $\mu_{\text{T}}$  ( $\mu_{\text{B}}$ ) is the top (bottom) layer chemical potential referenced to charge neutrality.

Figure 1(d) shows  $g_{\text{Int}}$  calculated for the biasing conditions of Fig. 1(c). An interlayer coupling of  $t = 1.0$   $\mu\text{eV}$  best fits the measurements. Figure 1(e) shows the calculated bands of the top and bottom graphene layers corresponding to the regimes labeled in Fig. 1(c). At points (i) and (ii) a peak in interlayer conductance occurs because the energy bands are aligned. At points (iii) and (iv) the bands are energetically misaligned, suppressing the interlayer tunneling. Figure 1(f) shows  $g_{\text{Int}}$  vs.  $V_{\text{Int}}$  measured at  $V_{\text{TG}}$  and  $V_{\text{BG}}$  values with the resonant peak at  $V_{\text{Int}} = 0$  V. A fit of the experimental data yields

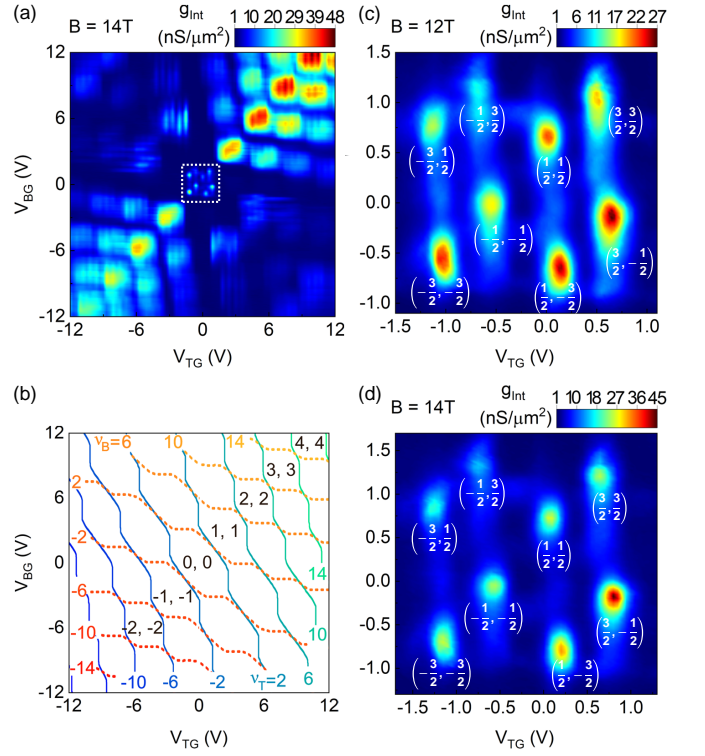


FIG. 2. (a)  $g_{\text{Int}}$  vs.  $V_{\text{TG}}$  and  $V_{\text{BG}}$  measured at  $V_{\text{Int}} = 0$  V,  $B = 14$  T, and  $T = 1.5$  K. The dotted line marks the  $N_{\text{T}} = N_{\text{B}} = 0$  LL. (b) Calculated LL occupancy in each layer at  $B = 14$  T. The integers mark the orbital LL indices. (c)–(d)  $g_{\text{Int}}$  vs.  $V_{\text{TG}}$  and  $V_{\text{BG}}$  within the  $N_{\text{T}} = N_{\text{B}} = 0$  sector, at  $B = 12$  T [panel (c)] and  $B = 14$  T [panel (d)]. The  $g_{\text{Int}}$  maxima are labeled by their layer fillings ( $\nu_{\text{T}}, \nu_{\text{B}}$ ).

$\Gamma = 33$  meV. The  $\Gamma$  values increase slightly with the layer density (see Fig. S1 of Supplemental Material). To assess the rotational alignment between the two layers, we performed calculations similar to Fig. 1(d) data, but including a twist between the two layers. A comparison with experimental data indicate the alignment is within  $0.2^\circ$  (see Fig. S2 and Fig. S3 of Supplemental Material).

In a perpendicular magnetic field ( $B$ ) the electrons occupy LLs, with a fourfold, spin and valley degeneracy in the absence of interactions [23, 24]. In Fig. 2(a), we plot  $g_{\text{Int}}$  measured at  $V_{\text{Int}} = 0$  V as a function of  $V_{\text{TG}}$  and  $V_{\text{BG}}$  at  $B = 14$  T, and  $T = 1.5$  K (see Supplemental Material Fig. S4 for data measured at  $B = 3$  T). The data show  $g_{\text{Int}}$  oscillations vs.  $V_{\text{TG}}$  and  $V_{\text{BG}}$ , associated with LLs in both layers. To understand Fig. 2(a) data, we employ Eqs. (4–5) and  $\mu(N) = \text{sgn}(N)v_F\sqrt{2e\hbar B|N|}$ , where  $N$  is the highest occupied orbital LL index. Figure 2(b) shows the LL filling factor  $\nu_{\text{T}}$  ( $\nu_{\text{B}}$ ) in the top (bottom) layer, and the top (bottom) layer orbital LL indices  $N_{\text{T}}$  ( $N_{\text{B}}$ ) along the  $n_{\text{T}} = n_{\text{B}}$  diagonal. We determine  $C_{\text{TG}} = 88$  nF/cm<sup>2</sup>,  $C_{\text{BG}} = 78$  nF/cm<sup>2</sup>, and  $C_{\text{Int}} = 1.5$   $\mu\text{F}/\text{cm}^2$ . The model accurately captures the experimental  $g_{\text{Int}}$  oscillations, with minima at

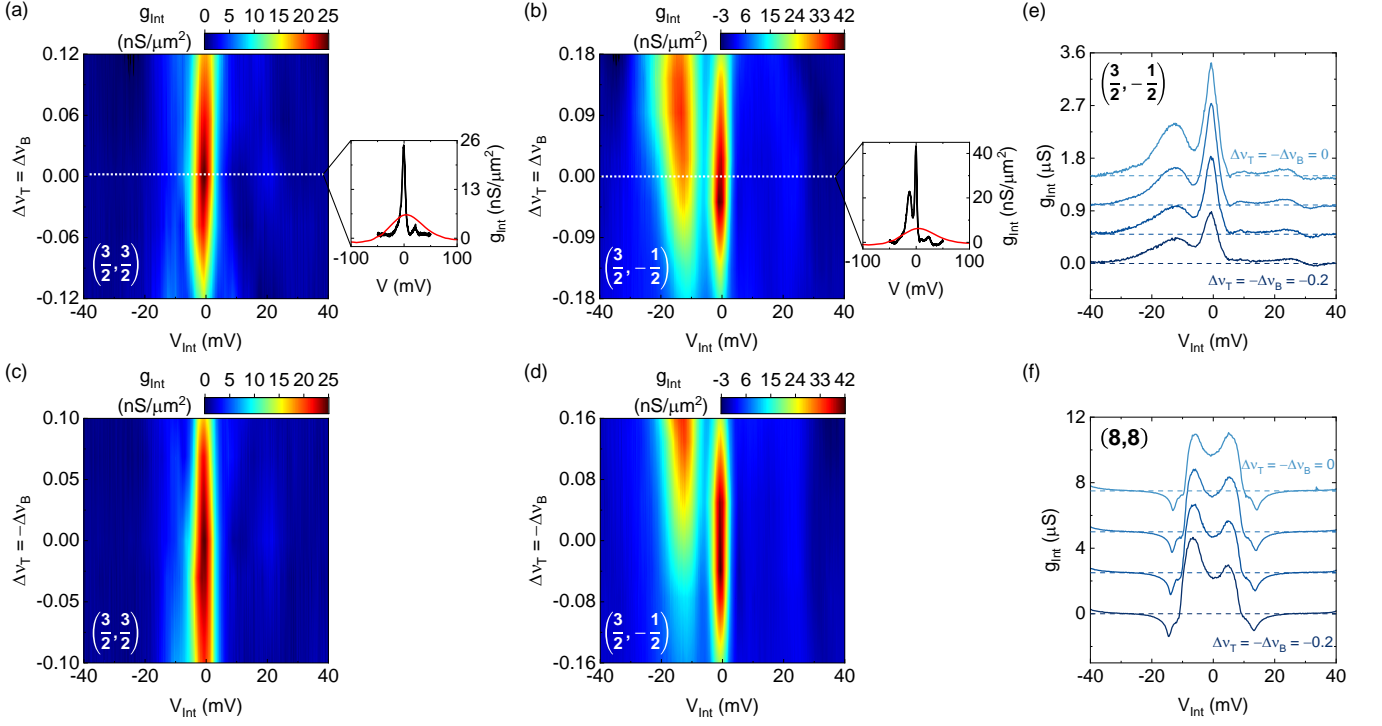


FIG. 3. (a)–(b)  $g_{\text{Int}}$  vs.  $V_{\text{Int}}$  and  $\Delta\nu_T = \Delta\nu_B$  measured at  $B = 14$  T and  $T = 1.5$  K for (a)  $(\nu_T, \nu_B) = (3/2, 3/2)$ , and (b)  $(\nu_T, \nu_B) = (3/2, -1/2)$ . The insets show  $g_{\text{Int}}$  vs.  $V_{\text{Int}}$  for  $\Delta\nu_T = \Delta\nu_B = 0$  at  $B = 14$  T (black) and  $g_{\text{Int}}$  vs. interlayer electrostatic potential difference at  $B = 0$  T (red). (c)–(d)  $g_{\text{Int}}$  vs.  $V_{\text{Int}}$  and  $\Delta\nu_T = -\Delta\nu_B$  measured at  $B = 14$  T and  $T = 1.5$  K for (c)  $(\nu_T, \nu_B) = (3/2, 3/2)$ , and (d)  $(\nu_T, \nu_B) = (3/2, -1/2)$ . (e)–(f)  $g_{\text{Int}}$  vs.  $V_{\text{Int}}$  at select  $\Delta\nu_T = -\Delta\nu_B$  for (e)  $(\nu_T, \nu_B) = (3/2, -1/2)$  and (f)  $(\nu_T, \nu_B) = (8, 8)$ . The traces are offset for clarity. The dashed lines mark  $g_{\text{Int}} = 0$ .

$\nu_{T,B} = \dots, -10, -6, -2, 2, 6, 10, \dots$ , consistent with a single-particle picture where  $g_{\text{Int}}$  minima (maxima) occur under full (partial) orbital LL fillings due to the availability of extended states.

In Figs. 2(c) and 2(d), we highlight  $g_{\text{Int}}$  as a function of  $V_{\text{TG}}$  and  $V_{\text{BG}}$  with  $V_{\text{Int}} = 0$  and  $T = 1.5$  K, inside the  $N_T = N_B = 0$  sector for  $B = 12$  and  $B = 14$  T respectively. Along the  $n_T = n_B$  diagonal we observe clear  $g_{\text{Int}}$  maxima at  $(\nu_T, \nu_B) = (\pm 3/2, \pm 3/2)$  and  $(\pm 1/2, \pm 1/2)$ , where both the top and bottom filling factors  $\nu_T$  and  $\nu_B$  are equal half-integers. The states  $(\nu_T, \nu_B) = (\pm 3/2, \pm 3/2)$  correspond to a total filling factor of  $\nu = \nu_T + \nu_B = \pm 3$ , and  $(\nu_T, \nu_B) = (\pm 1/2, \pm 1/2)$  correspond to  $\nu = \pm 1$ . In addition, we observe  $g_{\text{Int}}$  maxima at  $(\nu_T, \nu_B) = (\pm 3/2, \mp 1/2)$  and  $(\pm 1/2, \mp 3/2)$ , corresponding to the imbalanced state at  $\nu = \pm 1$ . No peaks are observed at  $(\nu_T, \nu_B) = (\pm 3/2, \pm 1/2)$  or  $(\pm 1/2, \pm 3/2)$ . Figures 2(c) and 2(d) data depart markedly from observations made in  $|N| > 0$  LLs, where no  $g_{\text{Int}}$  peaks are observed when the layers are at half LL filling factors.

A mechanism that leads to enhanced  $g_{\text{Int}}$  values is the formation of interlayer phase coherent QHSs. Indeed, at  $B = 14$  T the effective layer separation  $d/l_B = 0.29$  is sufficiently small that inter- and intralayer interaction become comparable;  $l_B = \sqrt{\hbar/eB}$  is the magnetic length.

These conditions are expected to lead to phase coherence between electrons in different layers, which manifests in the case of short range order [25–27] as an enhanced Josephson-like interlayer tunneling [6–8].

To shed light on the mechanisms leading to enhanced tunneling at many half-integer layer fillings in Fig. 3(a) we plot  $g_{\text{Int}}$  vs.  $V_{\text{Int}}$ , when we concomitantly vary  $\nu_T$  and  $\nu_B$  by equal amounts  $\Delta\nu_T = \Delta\nu_B$  away from  $(\nu_T, \nu_B) = (3/2, 3/2)$ . The inset shows  $g_{\text{Int}}$  vs.  $V_{\text{Int}}$  when  $\Delta\nu_T = \Delta\nu_B = 0$  (black), and  $g_{\text{Int}}$  vs. interlayer electrostatic potential difference at  $B = 0$  T (red), illustrating a much sharper zero-bias  $g_{\text{Int}}$  peak at  $B = 14$  T compared to the  $B = 0$  T data. A similar dataset measured for  $(\nu_T, \nu_B) = (3/2, -1/2)$  is shown in Fig. 3(b). Figures 3(c) and 3(d) show  $g_{\text{Int}}$  vs.  $V_{\text{Int}}$  and  $\Delta\nu_T = -\Delta\nu_B$  corresponding to  $(\nu_T, \nu_B) = (3/2, 3/2)$  and  $(\nu_T, \nu_B) = (3/2, -1/2)$ , respectively. Interestingly, for both  $(\nu_T, \nu_B) = (3/2, 3/2)$  and  $(3/2, -1/2)$ , corresponding to  $\nu = 3$  and  $\nu = 1$ ,  $g_{\text{Int}}$  peaks are observed at  $V_{\text{Int}} = 0$  with widths significantly smaller compared to the  $B = 0$  T resonances [see e.g. Fig. 1(f)]. The  $g_{\text{Int}}$  peak positions are stable at  $V_{\text{Int}} = 0$  V, and do not respond to layer filling factor variations. In contrast, the conductance in a noninteracting electron picture is proportional to an integral over energy of the layers density-of-states (DOS) product evaluated at  $E$  in one layer and

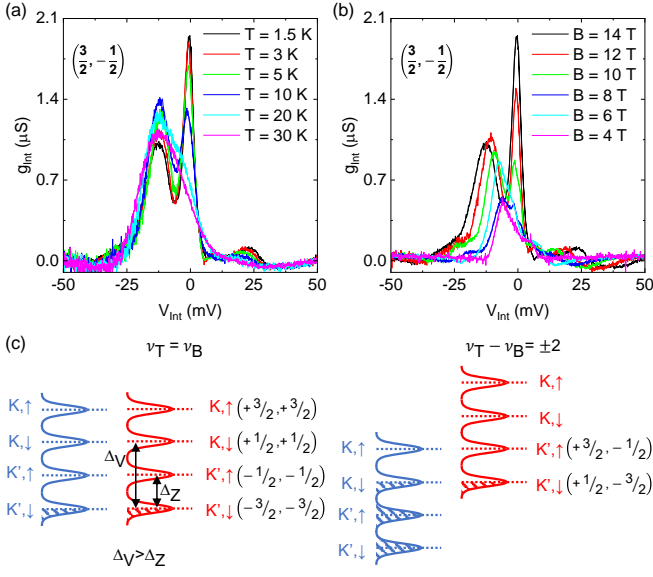


FIG. 4. (a)  $T$  dependence of  $g_{\text{Int}}$  vs.  $V_{\text{Int}}$  at  $B = 14$  T, for  $(\nu_T, \nu_B) = (3/2, -1/2)$ . (b)  $B$  dependence of  $g_{\text{Int}}$  vs.  $V_{\text{Int}}$  at  $T = 1.5$  K, for  $(\nu_T, \nu_B) = (3/2, -1/2)$ . (c) Schematic of the types of paired states observed.

$E + eV_{\text{Int}}$  in the other layer. This picture predicts zero-bias  $g_{\text{Int}}$  peaks only when the DOS is maximized at the Fermi level in both layers, a property that cannot be maintained over finite ranges of layer filling factors. Indeed, calculations of  $g_{\text{Int}}$  vs.  $V_{\text{Int}}$  and  $\Delta\nu_T = -\Delta\nu_B$  using a single-particle interlayer tunneling model for half-filled Landau levels (see Supplemental Material Fig. S5) show a  $g_{\text{Int}}$  peak that evolves with  $V_{\text{Int}}$ , in clear contrast to Fig. 3(a)–3(d) data.

The zero-bias  $g_{\text{Int}}$  peaks demonstrate the emergence of phase coherence between the two graphene monolayers at  $\nu = 1$  and  $\nu = 3$ , where electrons occupy a coherent superposition of states in both layers. We contrast the zero-bias  $g_{\text{Int}}$  peaks observed at  $\nu = 1$  and  $\nu = 3$  with measurements at  $\nu_T = \nu_B = 8$  in the half-filled  $N = 2$  sector. Figures 3(e) and 3(f) compare  $g_{\text{Int}}$  vs.  $V_{\text{Int}}$  and  $\Delta\nu_T = -\Delta\nu_B$  for  $(\nu_T, \nu_B) = (3/2, -1/2)$  and  $(8, 8)$  respectively. For the  $(\nu_T, \nu_B) = (8, 8)$  case we observe  $g_{\text{Int}}$  minima at  $V_{\text{Int}} = 0$ , as opposed to a peak, consistent with a tunneling gap at the Fermi level, similar to the suppression of tunneling between two half-filled uncorrelated LLs [28, 29]. We observe similar  $g_{\text{Int}}$  minima at  $V_{\text{Int}} = 0$  at other half-filled LLs outside the  $N = 0$  sector, suggesting that interlayer phase coherence is present at  $\nu = \pm 1$  and  $\nu = \pm 3$ , but not elsewhere.

The temperature dependence of the  $g_{\text{Int}}$  vs.  $V_{\text{Int}}$  zero-bias peak present at  $(\nu_T, \nu_B) = (3/2, -1/2)$  is shown in Fig. 4(a). The zero-bias  $g_{\text{Int}}$  peak for  $(\nu_T, \nu_B) = (3/2, -1/2)$  decreases as  $T$  is increased. A similar decrease in  $g_{\text{Int}}$  peak height as temperature is increased is observed at other  $\nu = \pm 1$  and  $\pm 3$  states (see Supple-

mental Material Fig. S6). At  $T = 30$  K, the interlayer conductance at  $V_{\text{Int}} = 0$  with the background tunneling removed ( $\Delta g_{\text{Int}}$ ) vanishes, signaling the interlayer phase coherence is no longer present. The  $T$  dependence of  $g_{\text{Int}}$  is particularly interesting for  $(\nu_T, \nu_B) = (3/2, -1/2)$ , since the height of the zero-bias  $g_{\text{Int}}$  peak drops sharply with increasing temperature. In contrast, the  $g_{\text{Int}}$  side-peak at  $V_{\text{Int}} \neq 0$  remains present and broadens noticeably with increasing temperature, which suggests the zero-bias peak is driven by interlayer phase coherence in the many-body ground state, whereas the side-peak is not. Figure 4(b) shows the  $B$  dependence of the  $g_{\text{Int}}$  vs.  $V_{\text{Int}}$  at  $(\nu_T, \nu_B) = (3/2, -1/2)$ . Reducing  $B$  from 14 T to 4 T corresponds to varying  $d/l_B$  from 0.29 to 0.16, which renders the double layer more interacting. However, the zero-bias  $g_{\text{Int}}$  peak for  $(\nu_T, \nu_B) = (3/2, -1/2)$  decreases as  $B$  is decreased, and is extinguished at  $B = 6$  T, likely because of static disorder.

Order in the interlayer electron-hole pair amplitude can be viewed as layer pseudospin ( $\vec{m}$ ) ferromagnetism with order in the  $\hat{x} - \hat{y}$  plane. The layers' chemical potential difference is then  $\propto m_z$ , where  $m_z$  is the pseudospin component along the  $z$  axis. According to the layer ferromagnet Landau-Lifshitz equations, it follows that nonequilibrium steady states with a fixed bias voltage are unstable to states with oscillatory collective dynamics. The enhanced tunneling seen experimentally in semiconductor quantum wells [6–8] have been consistently interpreted as evidence for states with nascent order that has finite temporal and/or spatial range [25–27]. The conductance due to enhanced short-range interlayer coherence is always peaked at zero bias, in contrast to single-particle resonant conductance peaks.

Because interlayer coherence is observed for  $\nu_T = \nu_B$  and  $\nu_T - \nu_B = \pm 2$ , two types of paired states can be pictured [Fig. 4(c)]. We assume that valley and spin degeneracy in the  $N = 0$  LL is lifted such that the valley splitting ( $\Delta_V$ ) dominates over the Zeeman effect ( $\Delta_Z$ ) leading to a valley polarized  $\nu = 0$  QHS in each layer [30]. The observation of interlayer coherence at both  $\nu_T = \nu_B$  and  $\nu_T - \nu_B = \pm 2$  is consistent with spin conservation in interlayer tunneling. The absence of tunneling at  $\nu_T - \nu_B = \pm 1, 3$  is expected since single-particle spin-flip tunneling is expected to be extremely weak in graphene, and does imply that interlayer coherence is absent in these cases. If valley is also conserved in tunneling, the observation of interlayer coherence at  $\nu_T - \nu_B = \pm 2$  implies that the valley splitting in the  $N = 0$  LL does not lead to  $\mathbf{K}$  and  $\mathbf{K}'$  states associated with the two sublattices of monolayer graphene, but rather a valley superposition [31, 32].

Josephson-like interlayer tunneling associated with coherence in interacting double layers require single-particle tunneling because the critical current  $I_0 \propto t^2$  [25, 27]. In twist-misaligned double layers single particle tunneling is suppressed because of the momentum

mismatch between the band minima. The twist-aligned graphene double layer sample design ensures that single particle tunneling is not suppressed, and establishes twist control as key to probing interlayer coherence by identifying tunneling anomalies in double layers of two-dimensional materials.

We thank Timo Hyart for useful discussions. The work at The University of Texas was supported by the National Science Foundation Grants No. EECS-2122476 and No. DMR-1720595, Army Research Office under Grant No. W911NF-17-1-0312. Work was partly done at the Texas Nanofabrication Facility supported by NSF Grant No. NNCI-1542159 and at the Texas Advanced Computing Center (TACC) at The University of Texas at Austin. K.W. and T.T. acknowledge support from the Elemental Strategy Initiative conducted by the MEXT, Japan (Grant No. JPMXP0112101001) and JSPS KAKENHI (Grant Nos. JP19H05790 and No. JP20H00354). K.U. acknowledges support from the JSPS KAKENHI Grants No. JP25107004, No. JP18H01822, No. JP21K04826, and No. JP22H05445.

---

\* Corresponding Author: etutuc@mail.utexas.edu

- [1] Y. W. Suen, L. W. Engel, M. B. Santos, M. Shayegan, and D. C. Tsui, *Phys. Rev. Lett.* **68**, 1379 (1992).
- [2] J. P. Eisenstein, G. S. Boebinger, L. N. Pfeiffer, K. W. West, and S. He, *Phys. Rev. Lett.* **68**, 1383 (1992).
- [3] D. R. Luhman, W. Pan, D. C. Tsui, L. N. Pfeiffer, K. W. Baldwin, and K. W. West, *Phys. Rev. Lett.* **101**, 266804 (2008).
- [4] J. Shabani, T. Gokmen, Y. T. Chiu, and M. Shayegan, *Phys. Rev. Lett.* **103**, 256802 (2009).
- [5] J. Eisenstein, *Annual Review of Condensed Matter Physics* **5**, 159 (2014).
- [6] I. B. Spielman, J. P. Eisenstein, L. N. Pfeiffer, and K. W. West, *Phys. Rev. Lett.* **84**, 5808 (2000).
- [7] L. Tiemann, Y. Yoon, W. Dietsche, K. von Klitzing, and W. Wegscheider, *Phys. Rev. B* **80**, 165120 (2009).
- [8] D. Nandi, T. Khaire, A. D. K. Finck, J. P. Eisenstein, L. N. Pfeiffer, and K. W. West, *Phys. Rev. B* **88**, 165308 (2013).
- [9] M. Kellogg, J. P. Eisenstein, L. N. Pfeiffer, and K. W. West, *Phys. Rev. Lett.* **93**, 036801 (2004).
- [10] E. Tutuc, M. Shayegan, and D. A. Huse, *Phys. Rev. Lett.* **93**, 036802 (2004).
- [11] R. D. Wiersma, J. G. S. Lok, S. Kraus, W. Dietsche, K. von Klitzing, D. Schuh, M. Bichler, H.-P. Tranitz, and W. Wegscheider, *Phys. Rev. Lett.* **93**, 266805 (2004).
- [12] D. Nandi, A. D. K. Finck, J. P. Eisenstein, L. N. Pfeiffer, and K. W. West, *Nature* **488**, 481 (2012).
- [13] A. D. K. Finck, J. P. Eisenstein, L. N. Pfeiffer, and K. W. West, *Phys. Rev. Lett.* **106**, 236807 (2011).
- [14] X. Liu, K. Watanabe, T. Taniguchi, B. I. Halperin, and P. Kim, *Nature Phys* **13**, 746 (2017).
- [15] J. I. A. Li, T. Taniguchi, K. Watanabe, J. Hone, and C. R. Dean, *Nature Phys* **13**, 751 (2017).
- [16] C. R. Dean, A. F. Young, I. Meric, C. Lee, L. Wang, S. Sorgenfrei, K. Watanabe, T. Taniguchi, P. Kim, K. L. Shepard, and J. Hone, *Nature Nanotech* **5**, 722 (2010).
- [17] K. Kim, M. Yankowitz, B. Fallahazad, S. Kang, H. C. P. Movva, S. Huang, S. Larentis, C. M. Corbet, T. Taniguchi, K. Watanabe, S. K. Banerjee, B. J. LeRoy, and E. Tutuc, *Nano Letters* **16**, 1989 (2016).
- [18] L. Britnell, R. V. Gorbachev, A. K. Geim, L. A. Ponomarenko, A. Mishchenko, M. T. Greenaway, T. M. Fromhold, K. S. Novoselov, and L. Eaves, *Nat Commun* **4**, 1794 (2013).
- [19] A. Mishchenko, J. S. Tu, Y. Cao, R. V. Gorbachev, J. R. Wallbank, M. T. Greenaway, V. E. Morozov, S. V. Morozov, M. J. Zhu, S. L. Wong, F. Withers, C. R. Woods, Y.-J. Kim, K. Watanabe, T. Taniguchi, E. E. Vdovin, O. Makarovskiy, T. M. Fromhold, V. I. Falko, A. K. Geim, L. Eaves, and K. S. Novoselov, *Nature Nanotech* **9**, 808 (2014).
- [20] B. Fallahazad, K. Lee, S. Kang, J. Xue, S. Larentis, C. Corbet, K. Kim, H. C. P. Movva, T. Taniguchi, K. Watanabe, L. F. Register, S. K. Banerjee, and E. Tutuc, *Nano Letters* **15**, 428 (2015).
- [21] G. W. Burg, N. Prasad, B. Fallahazad, A. Valsaraj, K. Kim, T. Taniguchi, K. Watanabe, Q. Wang, M. J. Kim, L. F. Register, and E. Tutuc, *Nano Letters* **17**, 3919 (2017).
- [22] G. W. Burg, N. Prasad, K. Kim, T. Taniguchi, K. Watanabe, A. H. MacDonald, L. F. Register, and E. Tutuc, *Phys. Rev. Lett.* **120**, 177702 (2018).
- [23] K. S. Novoselov, A. K. Geim, S. V. Morozov, D. Jiang, M. I. Katsnelson, I. V. Grigorieva, S. V. Dubonos, and A. A. Firsov, *Nature* **438**, 197 (2005).
- [24] Y. Zhang, Y.-W. Tan, H. L. Stormer, and P. Kim, *Nature* **438**, 201 (2005).
- [25] A. Stern, S. M. Girvin, A. H. MacDonald, and N. Ma, *Phys. Rev. Lett.* **86**, 1829 (2001).
- [26] D. V. Fil and S. I. Shevchenko, *Journal of Physics: Condensed Matter* **21**, 215701 (2009).
- [27] T. Hyart and B. Rosenow, *Phys. Rev. B* **83**, 155315 (2011).
- [28] J. P. Eisenstein, L. N. Pfeiffer, and K. W. West, *Phys. Rev. Lett.* **69**, 3804 (1992).
- [29] P. Johansson and J. M. Kinaret, *Phys. Rev. Lett.* **71**, 1435 (1993).
- [30] A. F. Young, C. R. Dean, L. Wang, H. Ren, P. Cadden-Zimansky, K. Watanabe, T. Taniguchi, J. Hone, K. L. Shepard, and P. Kim, *Nature Phys* **8**, 550 (2012).
- [31] X. Liu, G. Farahi, C.-L. Chiu, Z. Papic, K. Watanabe, T. Taniguchi, M. P. Zaletel, and A. Yazdani, *Science* **375**, 321 (2022).
- [32] A. Coissard, D. Wander, H. Vignaud, A. G. Grushin, C. Repellin, K. Watanabe, T. Taniguchi, F. Gay, C. B. Winkelmann, H. Courtois, H. Sellier, and B. Sacépé, *Nature* **605**, 51 (2022).

# Supplemental Material for Emergence of Interlayer Coherence in Twist-Controlled Graphene Double Layers

Kenneth A. Lin, Nitin Prasad, G. William Burg, Bo Zou, Keiji Ueno, Kenji Watanabe, Takashi Taniguchi, Allan H. MacDonald, and Emanuel Tutuc

## I. Quasiparticle state energy broadening

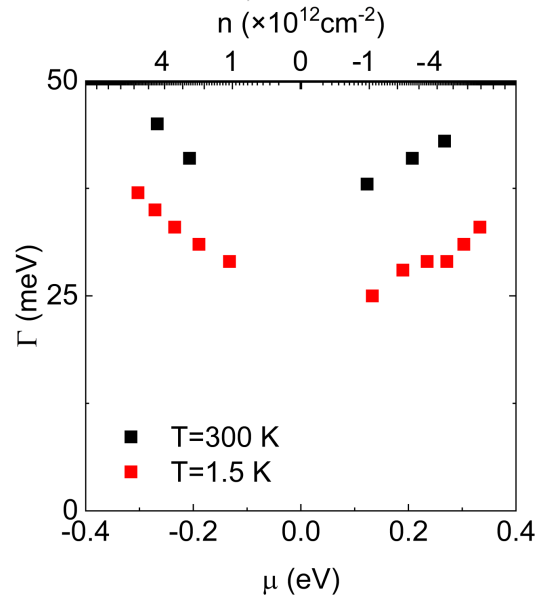


FIG. S1. Quasiparticle state energy broadening ( $\Gamma$ ) for resonances at  $V_{\text{Int}} = 0$  V under no applied magnetic field, as a function of energy  $\mu$  referenced to the Dirac point of the graphene layers (bottom axis) and concentration (top axis). A fit of Eqs. 1–3 in the main text to experimental data yields  $\Gamma$ .

## II. Interlayer tunneling in the presence of a twist between the two layers crystal axes

When a small twist angle between the graphene layers is present, the K points of the two layers are shifted relative to each other by an amount proportional to the twist angle  $\Delta\mathbf{K} = \hat{z} \times \theta\mathbf{K}$ ; this in turn introduces a momentum shift  $\hbar\Delta\mathbf{K}$  to the tunneling carriers [1]. The momentum shift introduced by the twist angle is similar to applying an in-plane magnetic field [2]. Even a small twist angle between the top and bottom graphene layers is expected to alter tunneling characteristics significantly [3]. At  $B = 0$  T with no perpendicular magnetic field applied, the momentum shift is expected to first broaden and then split the single primary resonant tunneling conductance peak into two resonance peaks, because the momentum difference is compensated by energetically shifting the two graphene layers Dirac cones by an amount  $\hbar v_F \Delta\mathbf{K}$  [1], where  $v_F$  is the Fermi velocity.

To assess the relative twist between the layer crystal axes in our sample, we compare the measured  $g_{\text{Int}}$  vs.  $V_{\text{Int}}$  and  $V_{\text{BG}}$  at a fixed  $V_{\text{TG}} = -2$  V [Fig. S2(a)] to calculations for different values of  $\theta$  [Fig. S2(b)–(e)]. For  $\theta \leq 0.2^\circ$ , the  $g_{\text{Int}}$  vs.  $V_{\text{Int}}$  and  $V_{\text{BG}}$  characteristics do not change significantly. However, as highlighted by the dashed lines in Fig. S2(b)–(e), when  $\theta$  increases beyond  $0.2^\circ$ , the primary resonance broadens and gets reduced in magnitude, as it is replaced by two resonances with an increasing separation in  $V_{\text{Int}}$  as the twist angle increases. From the comparison of measured data with calculations, we determine that the two graphene layer crystal axes are aligned within  $0.2^\circ$ .

To further illustrate the effect of an interlayer twist, Fig. S3(a) shows the measured  $g_{\text{Int}}$  vs.  $V_{\text{Int}}$  and  $V_{\text{TG}}$  at a fixed  $V_{\text{BG}} = 1$  V in a separate double monolayer graphene device using bilayer  $\text{WSe}_2$  as tunnel barrier, and  $\theta = 0.7^\circ$ . The data shows two tunneling resonances which evolve with  $V_{\text{Int}}$  and  $V_{\text{TG}}$ . By identifying the location of the two interlayer biases  $V_B$  at which the two layers Dirac cones begin to overlap, we can estimate  $\theta = 0.7^\circ$  in this additional device using  $eV_B \approx 2\hbar v_F \Delta\mathbf{K}$  where  $e$  is the electron charge. Furthermore, we find a good agreement between the measured data and calculation for the same value  $\theta = 0.7^\circ$  [Fig. S3(b)]. These datasets illustrate a method to assess if a relative twist exists between the layer crystal axes, and estimate its value.

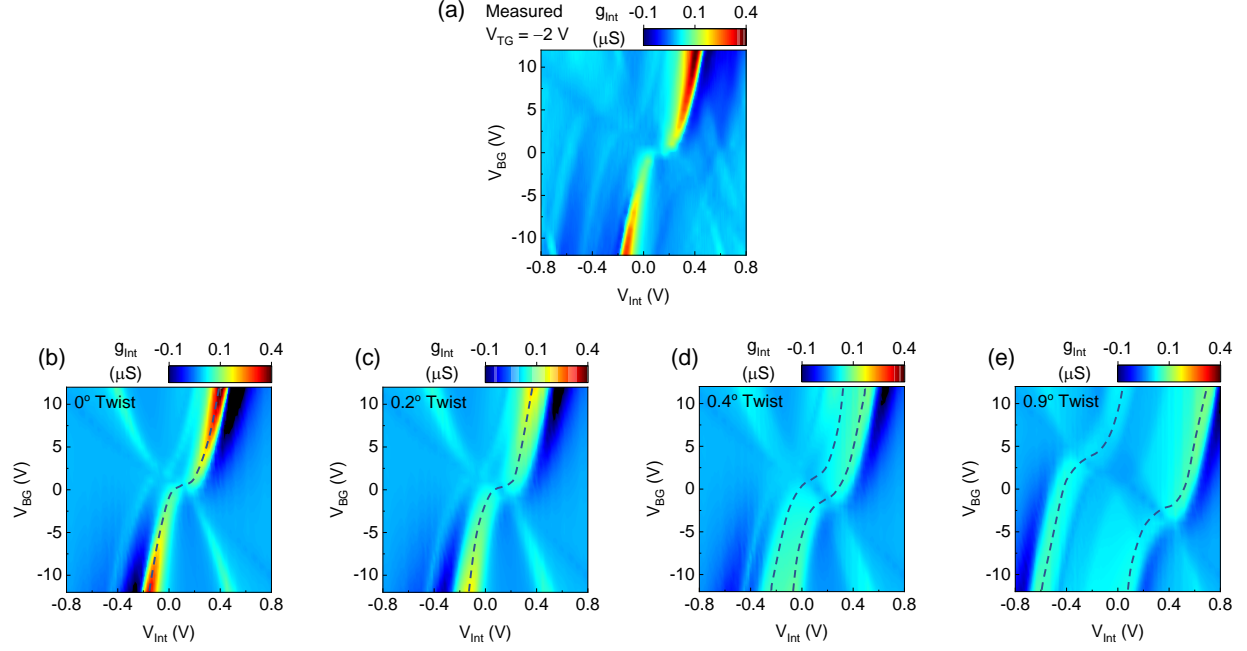


FIG. S2. (a) Measured  $g_{\text{Int}}$  vs.  $V_{\text{Int}}$  and  $V_{\text{BG}}$  at a fixed  $V_{\text{TG}} = -2$  V. (b)-(e) Calculated  $g_{\text{Int}}$  for different values of  $\theta$ . The dashed lines indicate the single primary resonant tunneling conductance peak broadens and then splits into two as twist angle increases.

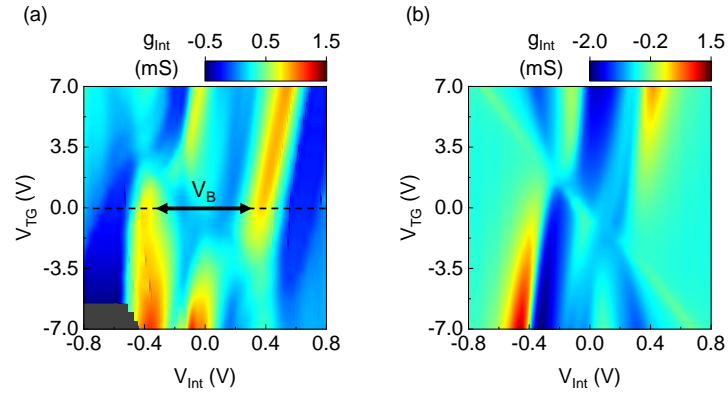


FIG. S3. (a) Measured  $g_{\text{Int}}$  vs.  $V_{\text{Int}}$  and  $V_{\text{TG}}$  at a fixed  $V_{\text{BG}} = 1$  V for an additional device with  $\theta = 0.7^\circ$ . (b) Calculated  $g_{\text{Int}}$  for the same biasing conditions as in panel (a), and  $\theta = 0.7^\circ$ .



### III. Quantum oscillations in tunneling conductance at low magnetic fields

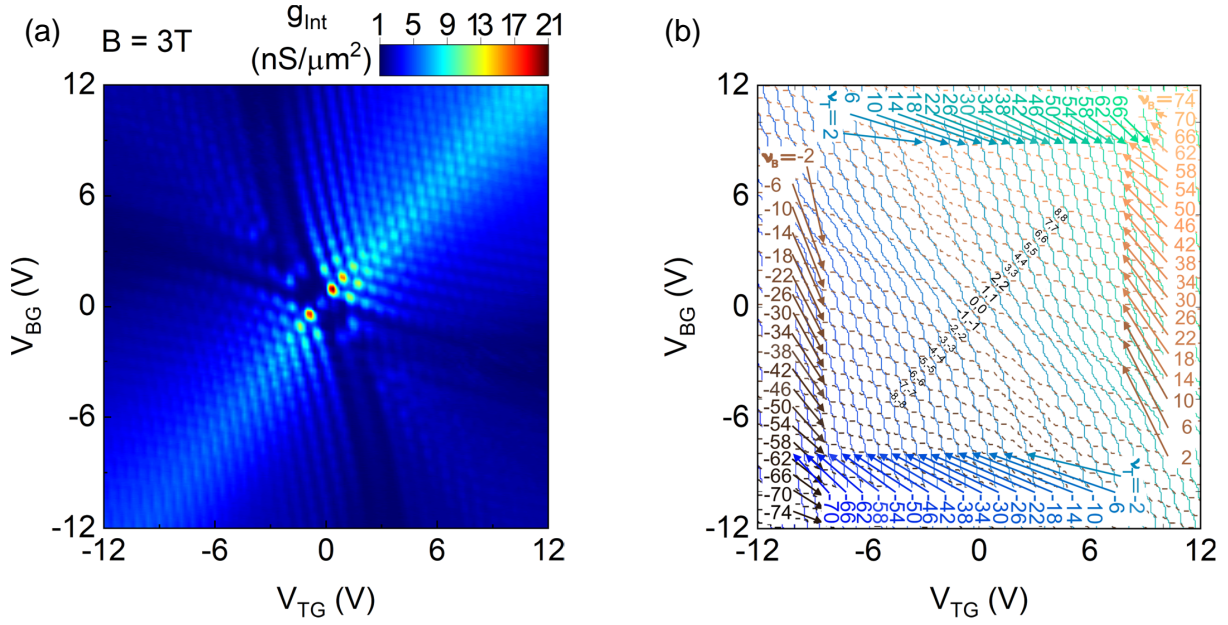


FIG. S4. (a)  $g_{\text{Int}}$  vs.  $V_{\text{TG}}$  and  $V_{\text{BG}}$  measured at  $V_{\text{Int}} = 0$  V,  $B = 3$  T, and  $T = 1.5$  K. (b) Calculated Landau level occupancy in each layer at  $B = 3$  T. The integers mark the four-fold degenerate orbital Landau level indices.

#### IV. Tunneling between uncorrelated landau levels

In Fig. S5, we use a single-particle tunneling model to rule out the scenario where extended states in individual, but otherwise uncorrelated layers lead to the observed zero-bias  $g_{\text{Int}}$  peak when the layers are at half-filling. The single particle tunneling between LLs of two graphene layers can be described using a model similar to that described in Eqs. (1)-(5) of the main text. We consider the tunneling process to strictly conserve the LL index  $N$  and spin  $\sigma$ . However, we allow relaxation of valley degree of freedom  $\sigma_v$  during tunneling. At high magnetic fields, the degeneracies in the LLs are lifted and the LL splitting is particularly prominent for  $N = 0$  and  $N = 1$  [4–6]. The tunneling rate in the presence of high magnetic fields is therefore given by

$$T(E) = \frac{A_{ov}}{h} \sum_{N;\sigma,\sigma_{vT},\sigma_{vB}} |t|^2 A_T(N, \sigma, \sigma_{vT}) A_B(N, \sigma, \sigma_{vB}). \quad (1)$$

Here,  $A(N, \sigma, \sigma_v)$  is the Lorentizan-broadened spectral density function of the LL given by

$$A(N, \sigma, \sigma_v) = \frac{eB_{\perp}}{\pi h} \frac{\Gamma}{(E - \epsilon(N, \sigma, \sigma_v))^2 + \Gamma^2}, \quad (2)$$

where  $\epsilon(N, \sigma, \sigma_v)$  are the discretized LL energies,  $B_{\perp}$  is the magnetic field applied entirely perpendicular to the sample and  $A_{ov}$  is the overlap area between the top and bottom graphene layers.

The experimental zero-bias  $g_{\text{Int}}$  peaks shown in the insets of Fig. 3(a) and (b) are significantly sharper in high-magnetic fields compared to the  $B = 0$  T data. Indeed, the single-particle model leads to a  $g_{\text{Int}}$  peak as a function of  $V_{\text{Int}}$  with a width similar to the experimental data of Fig. 3, only if using  $\Gamma = 2$  meV, a value that is more than ten-fold smaller compared to the  $\Gamma$  values of Figs. 1 and S3. Figure S5 shows the calculated  $g_{\text{Int}}$  vs.  $V_{\text{Int}}$  and  $\Delta\nu_T = -\Delta\nu_B$  using this model for half-filled Landau levels. The single-particle model shows a  $g_{\text{Int}}$  peak that evolves with  $V_{\text{Int}}$ , in clear contrast to experimental observations of Fig. 3(a-e) in the main text.

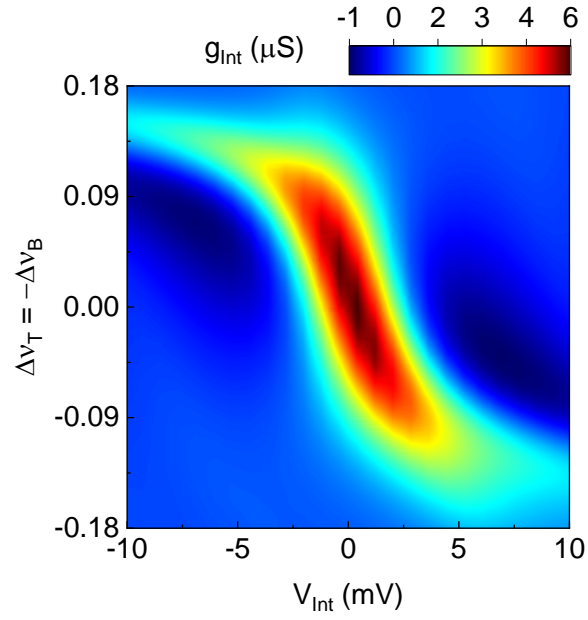


FIG. S5. Calculated  $g_{\text{Int}}$  vs.  $V_{\text{Int}}$  and  $\Delta\nu_T = -\Delta\nu_B$  at  $\nu = 3$  using a single-particle interlayer tunneling model, showing a  $g_{\text{Int}}$  peak that evolves with  $V_{\text{Int}}$ , in contrast to experimental observations.

V. Tunneling conductance dependence on magnetic field and temperature at  $\nu = \pm 1, \pm 3$

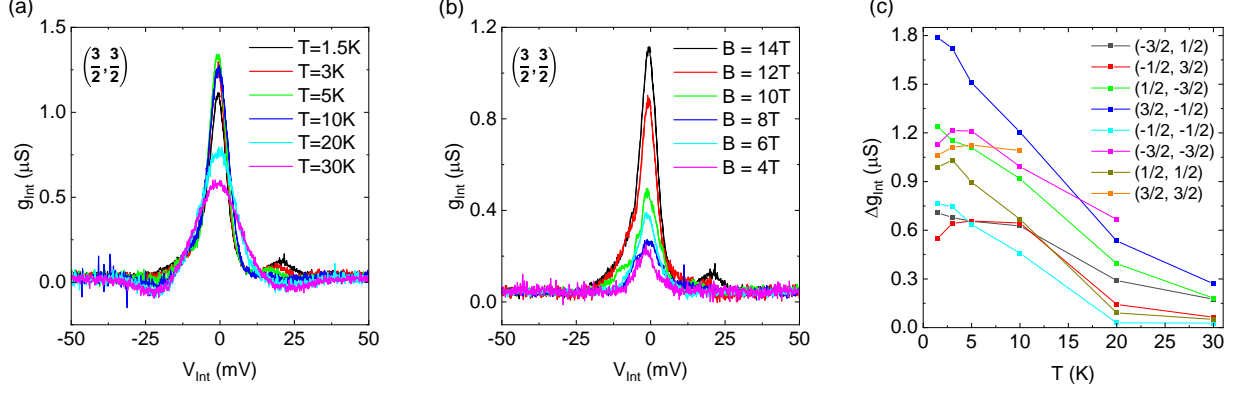


FIG. S6. (a)  $g_{\text{Int}}$  vs.  $V_{\text{Int}}$  at different  $T$  values, at  $B = 14$  T for  $(\nu_T, \nu_B) = (3/2, 3/2)$ . (b)  $B$ -dependence of  $g_{\text{Int}}$  vs.  $V_{\text{Int}}$  measured at  $T = 1.5$  K for  $(\nu_T, \nu_B) = (3/2, 3/2)$ . (c) Interlayer conductance with the background tunneling removed ( $\Delta g_{\text{Int}}$ ) at  $V_{\text{Int}} = 0$  vs.  $T$  measured at  $B = 14$  T for various  $\nu = \pm 1$  and  $\pm 3$  states.

- 
- [1] A. Mishchenko, J. S. Tu, Y. Cao, R. V. Gorbachev, J. R. Wallbank, M. T. Greenaway, V. E. Morozov, S. V. Morozov, M. J. Zhu, S. L. Wong, et al., *Nature Nanotech* **9**, 808 (2014), URL <https://doi.org/10.1038/nnano.2014.187>.
- [2] N. Prasad, G. W. Burg, K. Watanabe, T. Taniguchi, L. F. Register, and E. Tutuc, *Phys. Rev. Lett.* **127**, 117701 (2021), URL <https://link.aps.org/doi/10.1103/PhysRevLett.127.117701>.
- [3] W.-Y. He, Y. Su, M. Yang, and L. He, *Phys. Rev. B* **89**, 125418 (2014), URL <https://link.aps.org/doi/10.1103/PhysRevB.89.125418>.
- [4] Z. Jiang, Y. Zhang, H. L. Stormer, and P. Kim, *Phys. Rev. Lett.* **99**, 106802 (2007), URL <https://link.aps.org/doi/10.1103/PhysRevLett.99.106802>.
- [5] A. F. Young, C. R. Dean, L. Wang, H. Ren, P. Cadden-Zimansky, K. Watanabe, T. Taniguchi, J. Hone, K. L. Shepard, and P. Kim, *Nature Phys* **8**, 550 (2012), URL <https://doi.org/10.1038/nphys2307>.
- [6] S.-Y. Li, Y. Zhang, L.-J. Yin, and L. He, *Phys. Rev. B* **100**, 085437 (2019), URL <https://link.aps.org/doi/10.1103/PhysRevB.100.085437>.